ORIGINAL ARTICLE

# Continuous flow left ventricular pump support and its effect on regional left ventricular wall stress: finite element analysis study

**Choon-Sik Jhun · Kay Sun · Joshua P. Cysk**

**Abstract** Left ventricular assist device (LVAD) support unloads left ventricular (LV) pressure and volume and decreases wall stress. This study investigated the effect of systematic LVAD unloading on the 3-dimensional myocardial wall stress by employing finite element models containing layered fiber structure, active contractility, and passive stiffness. The HeartMate II® (Thoratec, Inc., Pleasanton, CA) was used for LV unloading. The model geometries and hemodynamic conditions for baseline (BL) and LVAD support ($LV_{support}$) were acquired from the Penn State mock circulatory cardiac simulator. Myocardial wall stress of BL was compared with that of $LV_{support}$ at 8,000, 9,000, 10,000 RPM, providing mean pump flow ($Q_{mean}$) of 2.6, 3.2, and 3.7 l/min, respectively. LVAD support was more effective at unloading during diastole as compared to systole. Approximately 40, 50, and 60 % of end-diastolic wall stress reduction were achieved at $Q_{mean}$ of 2.6, 3.2, and 3.7 l/min, respectively, as compared to only a 10 % reduction of end-systolic wall stress at $Q_{mean}$ of 3.7 l/min. In addition, there was a stress concentration during systole at the apex due to the cannulation and reduced boundary motion. This modeling study can be used to further understand optimal unloading, pump control, patient management, and cannula design.

C.-S. Jhun (✉) · J. P. Cysk
Division of Artificial Organs, Department of Surgery, College of Medicine, The Pennsylvania State University, 500 University Drive, Hershey, PA 17033, USA
e-mail: jcysk@hmc.psu.edu

K. Sun
Department of Biomedical Engineering, Vanderbilt University, Nashville, TN, USA

## 1 Introduction

The utility of left ventricular assist devices (LVADs) is prevailing in treating patients with end-stage heart failure. The primary application of an LVAD is to help a severely depressed left ventricle (LV) pump blood to the rest of the body. In addition, LVAD support reduces LV work load by lowering pressure and volume overload, which decreases LV wall stress [37].

An understanding of myocardial wall stress is crucial because it is closely related to regional coronary blood flow [16], myocardial oxygen consumption [9], hypertrophy [12], and cardiac molecular systems connected to the development of long-term cardiac insufficiency [37]. In LVAD applications, multiple studies found that chronic LVAD support reduces wall stress, and this may contribute to reverse remodeling [4, 38, 39]. LV wall stress quantified by Laplace's law may be useful in some clinical applications [6, 21, 25, 26, 36]; however, the global force balance approximation may not be suitable for understanding the wall stress distribution with LVAD support due to the alteration of local geometry at the apex and asymmetric boundary conditions. Thus, LV wall stress calculated based on Laplace's law may misrepresent myocardial wall stress [40].

Three-dimensional (3D) computational models of the LV with fiber structure implemented can simulate various cardio-physiologic conditions and predict 3D distribution of LV wall stress [18, 34, 35]. Using computational models previously developed [18, 34], this study quantified the

variation of 3D regional fiber stress distribution in the LV with continuous flow LVAD support. Finite element (FE) models were created based on hemodynamic parameters acquired from the Penn State cardiac simulator, and systematic changes in hemodynamic parameters over LVAD speed was used for the simulations. The 3D FE models include layered myocardial fiber structure, active contractility, and passive stiffness. Regional 3D wall stress distribution at each pump speed was calculated at end-diastole (ED) and end-systole (ES). In this study, we focused on testing a computational methodology for understanding regional 3D myocardial fiber stress in a LVAD-supported LV. This study modeled a partial dynamic cardiac cycle (i.e., filling and ejection phases only), and myocardial wall stresses were observed only at end-diastole and end-systole. The study took advantage of a controlled mock circulatory system that enables systematic measurements of LV geometry and pressure during pump support that is not easily available. Laplace-based LV wall stress was also observed at a medial plane where the short axis of the truncated ellipsoidal LV was located and compared with the FE-based wall stress.

## 2 Methods

### 2.1 Hemodynamic parameters and FE model construction

Hemodynamics of a given cardiac condition was achieved by using the Penn State mock cardiac simulator [19] with the HeartMate II axial flow LVAD [29]. The LV volumes and pressures were used to construct mathematical LV geometries and loading conditions, respectively. Table 1 lists hemodynamic parameters at baseline with no LVAD support (BL) and with LVAD support (LV$_{support}$) at pump speed of 8,000, 9,000, and 10,000 RPM, which provided mean pump flows ($Q_{mean}$) of 2.6, 3.2, and 3.7 l/min, respectively. LVAD pump speeds were selected to cover the standard clinical operating range [30]. Figure 1 shows hemodynamic waveforms of left ventricular pressure (LVP), aortic pressure (AoP), pump flow (Q), and left ventricular volume (LVV) for BL and 3 different levels of LV$_{support}$.

The reference (i.e., stress-free) LV geometry was modeled as a truncated prolate ellipsoid with dimensions based on the LV volume intercept ($V_0$) at null chamber pressure acquired from a family of pressure–volume loops (Fig. 2) [32]. The 3D geometry was constructed with 8 nodded hexahedral elements using a parametric meshing software TrueGrid® (XYZ Scientific Applications, Inc., Livermore, CA). The LV wall thickness at median plane and apex was 15 and 5 mm, respectively. Transmural variation in muscle fiber orientation and structural anisotropy are important features that contribute to end-diastolic and end-systolic

**Table 1** Hemodynamic parameters of BL and LV$_{support}$ acquired from the Penn state mock cardiac simulator

| Hemodynamic parameters | BL | LV$_{support}$, $Q_{mean}$ (l/min) | | |
|---|---|---|---|---|
| | | 2.6 | 3.2 | 3.7 |
| EDV (ml) | 88 | 83 | 81 | 78 |
| ESV (ml) | 67 | 62 | 61 | 59 |
| EDP (mmHg) | 12 | 10 | 9 | 8 |
| ESP (mmHg) | 95 | 93 | 93 | 91 |
| HR (BPM) | 80 | 80 | 80 | 80 |
| SV (ml) | 22 | 21 | 20 | 19 |
| EF (%) | 25 | 25 | 24 | 25 |
| SW (mmHg·ml) | 2,212 | 2,081 | 1,903 | 1,881 |
| AoP$_{mean}$ (mmHg) | 74 | 89 | 93 | 101 |
| Aortic valve condition | Open | Open | Open | Close |
| LVAD speed (RPM) | – | 8,000 | 9,000 | 10,000 |

*EDV* end-diastolic volume, *ESV* end-systolic volume, *EDP* end-diastolic pressure, *ESP* end-systolic pressure, *HR* heart rate, *SV* stroke volume, *EF* ejection fraction, *SW* stroke work, *AoP*$_{mean}$ mean aortic pressure, *Q*$_{mean}$ mean pump flow

fiber stress [14]. As such, the myocardial wall was refined into 3 elements transmurally, and myocardial muscle fiber structure throughout the LV was presumed to linearly vary in the transmural direction at 60° from the circumferential direction to the sub-endocardium, then at -60° from the circumferential direction to the epicardium (Fig. 3a) [18, 33]. The FE model of LV$_{support}$ (Fig. 3b) was created by penetrating the cannula tip to the apex of the BL model (Fig. 3a). The geometry of the cannula tip was acquired from the HeartMate II® inflow connector and modeled as a rigid body material (Young's modulus of 200 GPa and Poisson's ratio of 0.3) [11]. The model predictability was tested with a mesh refinement study in order to find the minimum number of elements needed to generate accurate results with minimal cost in computational time. The mesh convergence study determined that 2,592 elements (for BL) were sufficient, and additional mesh refinement resulted in only a 1 % variation of strain.

### 2.2 Loading and boundary conditions

End-diastolic and end-systolic LV pressures were applied outwards at the inner endocardial wall. The systematic variation of the LV pressures with increasing LVAD speed was applied for loading conditions for LV$_{support}$. Displacements of the epicardial nodes at the base were constrained in all directions. Thus, these nodes were used as a frame of reference for longitudinal, circumferential, and radial displacement. The endocardial and mid-wall basal nodes were free to move in the radial direction. Displacements of the shared nodes located in the interface between the sub-epicardium
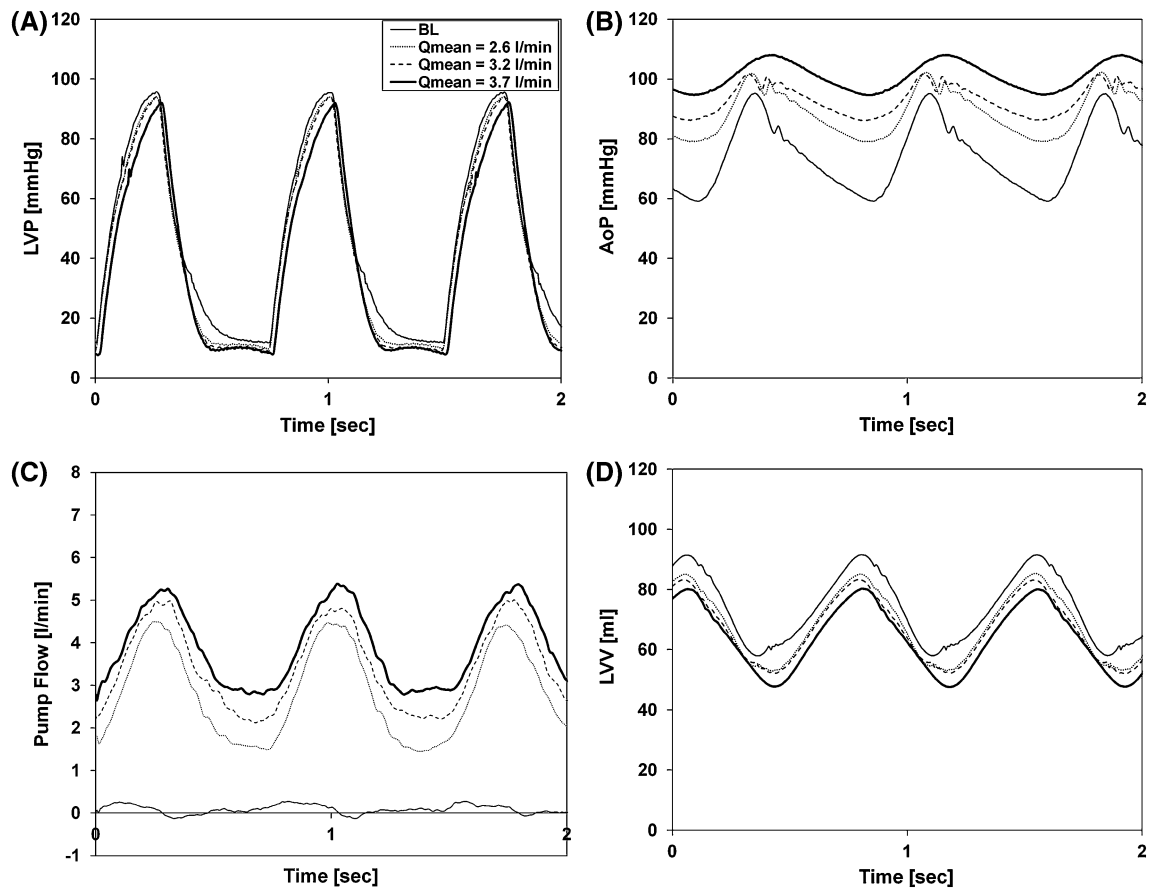
**Fig. 1** Hemodynamic waveforms of **a** left ventricular pressure (LVP). **b** aortic pressure (AoP). **c** pump flow (Q). **d** and left ventricular volume (LVV) for no pump support (BL) and LV$_{support}$ at Q of 2.6, 3.2, and 3.7 l/min
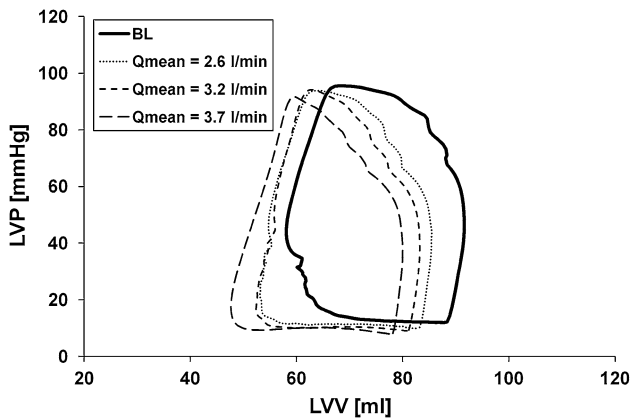


**Fig. 2** Pressure–volume loops of the BL and LV$_{support}$ at $Q_{mean}$ of 2.6, 3.2, and 3.7 l/min

and the cannula tip were constrained in the longitudinal direction: in practice, when cannulated, the ventricular apex is encircled with 4–6 felt-backed mattress sutures. A cruciate incision is made in the apex, and a tapered dilator is inserted into the ventricle. Upon removing the dilator, the

inlet cannula is rapidly but gently inserted into the ventricle and sutured in place through the felt flange where the outer interface between the sub-epicardium and cannula meet. A commercial explicit solver, LS-DYNA (LSTC, Inc., Livermore, CA) was used for a series of computational simulations. Due to the cannulation at the apex and wall thickness variation in long-axis direction, the LV was divided into 4 regions, i.e., upper (close to base), mid (median plane), lower (close to apex), and apex (circumferential interface between LV and cannula tip), and wall stress was reported in those areas.

### 2.3 Myocardial material properties for diastole and systole

Diastolic and systolic material properties of the myocardium were modeled as nearly incompressible, transversely isotropic, and hyperelastic (see "Appendix"). Material constants $b_f$, $b_t$, and $b_{fs}$ that govern the degree of anisotropy were chosen as 49.25, 19.25, and 17.44, respectively [34]. The material constant, $C$, was calibrated at 0.26 kPa, which produced the prescribed EDV at a given preload and material anisotropy values [18]. Systolic material properties

**Fig. 3** Finite element mesh of **a** BL and **b** LV$_{support}$
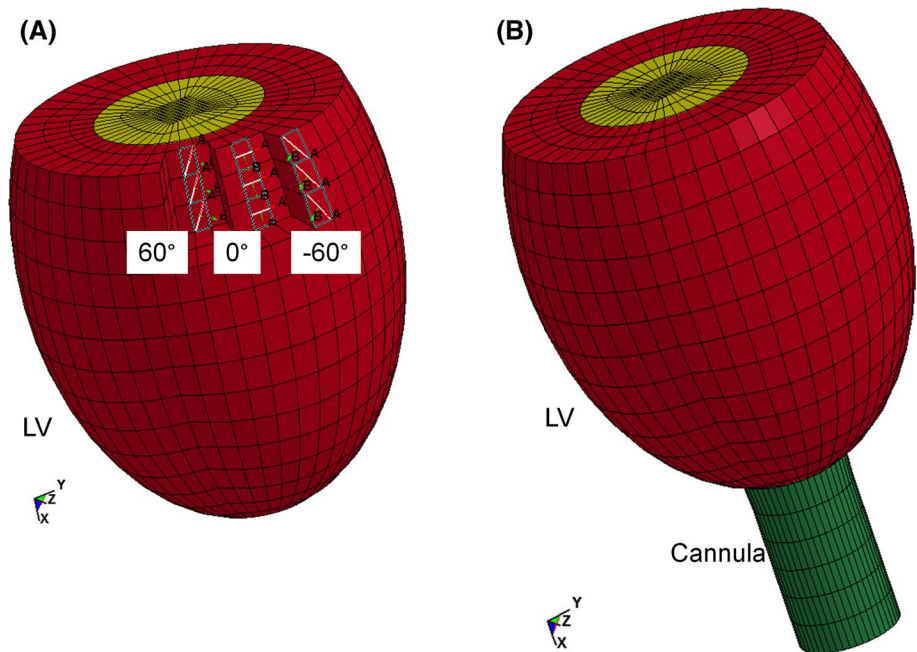


were selected to the following values: $Ca_0 = 4.35$ µmol/l, $(Ca_0)_{max} = 4.35$ µmol/l, $l_0 = 1.58$ µm, $m = 1.0\ 489$ s/µm, $b = -1.429$ s, $B = 4.75$ µm$^{-1}$, and $l_R = 1.85$ µm [18]. The contractility, $T_{max}$, was calibrated to be 126.4 kPa in order to achieve the prescribed ESV at a given afterload.

### 2.4 Effect of apical cannulation on LV wall stress

LVAD implantation with apical cannulation gives rise to local kinematic constraint at the apex. Regardless of the volumetric and pressure unloading by LVAD support, the apical constraint itself may cause a decrease in wall stress as shown in passive cardiac support devices for example [20, 22]. Thus, total wall stress reduction ($\Delta\sigma_{Total}$) by LVAD support can be described as:

$$\Delta\sigma_{Total} = \Delta\sigma_{PV} + \Delta\sigma_{AC} \tag{1}$$

where $\Delta\sigma_{PV}$ is the wall stress reduction contributed by pressure and volumetric unloading, and $\Delta\sigma_{AC}$ is the wall stress reduction contributed by the apical constraint. The reduction of wall stress for all LV$_{support}$ was characterized in terms of $\Delta\sigma_{PV}$ and $\Delta\sigma_{AC}$.

### 2.5 Laplace-based LV wall stress

Endocardial radii and wall thicknesses were obtained from a medial plane (i.e., Mid) where the short axis of the truncated ellipsoidal LV was located. Laplace-based LV wall stresses at a medial plane were calculated at end-diastole and end-systole from BL and each LVAD support condition.

### 2.6 Sensitivity study

To examine if the wall stress reduction at ED and ES at each level of LVAD support are sensitive to changes in diastolic and systolic material parameters, the cardiac condition of BL was greatly depressed by numerically reducing both myocardial compliance(by increasing $C$ in Eq. (1) in "Appendix")and contractility (by reducing $T_{max}$ in Eq. (2) in "Appendix") by 30 % ($C_{30} = 0.339$ kPa, $T_{max30} = 88.5$ kPa, EF = 15 %) from the material properties in BL. Two other scenarios were examined by reducing only (1) LV compliance by 10 % ($C_{10} = 0.287$ kPa), 30 % ($C_{30} = 0.339$ kPa), and 50 % ($C_{50} = 0.392$ kPa) from $C$ of 0.261 kPa while keeping $T_{max}$ constant as 126.4 kPa and (2) LV contractility by 10 % ($T_{max10} = 113.8$ kPa), 20 % ($T_{max20} = 101.1$ kPa), and 30 % ($T_{max30} = 88.5$ kPa) from $T_{max0}$ of 126.4 kPa while keeping $C$ constant as 0.261 kPa. The effect of diastolic material property ($C$) and systolic material property ($T_{max}$) on the reduction in wall stress occurred with LVAD support was examined with a one-sample $t$ test with the level of significance set at 0.05.

## 3 Results

### 3.1 Hemodynamics in computational simulation

Table 2 shows the LV volumes of the BL and LV$_{support}$ acquired by numerical simulations. The predictions of both the BL and LV$_{support}$ models are in close agreement

**Table 2** End-diastolic and end-systolic volumes obtained from numerical simulations

| LV volume | BL | LV$_{support}$, $Q_{mean}$ (l/min) | | |
| --- | --- | --- | --- | --- |
| | | 2.6 | 3.2 | 3.7 |
| EDV$_{Num}$ (ml) | 88 | 83 | 82 | 80 |
| ESV$_{Num}$ (ml) | 67 | 64 | 63 | 62 |

*EDV$_{Num}$* numerically acquired end-diastolic volume, *ESV$_{Num}$* numerically acquired end-systolic volume

with that of the data acquired from the cardiac simulator (Table 1).

### 3.2 LV wall stress distribution

FE analysis was able to show a localized 3D fiber stress distribution at end-diastole and end-systole throughout the LV wall. Figure 4 shows the cross-sectional view of the wall stress distribution at $Q_{mean}$ of 3.7 l/min. High wall stress was present at the apex at ED (Fig. 4a) and ES (Fig. 4b) of the LV$_{support}$. Similar patterns of wall stress distributions with different scales were observed at $Q_{mean}$ of 2.6 and 3.2 l/min. The wall stress at ED and ES of BL and LV$_{support}$ along the long-axis direction is shown in Fig. 5 for EF of 25 % (Fig. 5a, b) and 15 % (Fig. 5c, d). Note that Qnet = 0 represents the wall stress reduction achieved solely by the apical constraint (i.e., $\Delta\sigma_{AC}$ in Eq. 1). At EF of 25 % with initial LV mechanical material properties, the end-diastolic wall stress reduction ($\Delta\sigma_{Total}$) was 35 % (SD ± 16 %), 47 % (SD ± 10 %), and 59 % (SD ± 7 %) at $Q_{mean}$ of 2.6, 3.2, and 3.7 l/min, respectively (Fig. 5a). Note that 43 and 8 % of end-diastolic wall stress reduction at the apex and lower area, respectively, were achieved by the apical cannulation. The apical cannulation was not effective on mid

and upper areas. A slight decrease in end-systolic wall stress was observed with increasing LVAD support, but the amount of relative reduction was much smaller compared with that of end-diastole (Fig. 5b). With apical cannulation, end-systolic wall stress at the apex increased by 23 %, and even with the maximum support at $Q_{mean}$ of 3.7 l/min, end-systolic wall stress was still greater by 14 % than that of in BL. This stress concentration at the apex was due to the cannulation that constrained the apical motion during systole. However, the apical cannulation did not affect end-systolic wall stress at the lower, mid, and upper areas; in these areas, there was approximately 10 % reduction in end-systolic wall stress at $Q_{mean}$ of 3.7 l/min.

For further depressed model with EF of 15 % (Fig. 5c, d), all the results were quite similar. 37 % (SD ± 10 %), 45 % (SD ± 9 %), and 56 % (SD ± 6 %) of end-diastolic wall stress reduction were achieved at $Q_{mean}$ of 2.6, 3.2, and 3.7 l/min, respectively (Fig. 5c). The apical cannulation also gave rise to approximately 38 and 10 % of end-diastolic wall stress reduction at the apex and lower area, respectively. The effect of apical constraint at mid and upper areas was also trivial at end-diastole. Note that the apical cannulation caused approximately 8 % of wall stress increase at end-systole at the apex; however, increased end-systolic wall stress was nullified by maximum LVAD support. The effect of apical cannulation at lower, mid, and upper areas at end-systole was not noticeable. Similar to the EF = 25 % condition, there was approximately 10 % of end-systolic wall stress reduction at $Q_{mean}$ of 3.7 l/min in those regions. Laplace-based end-diastolic wall stress was found to be comparable with the FE-based LV wall stress at mid area, but Laplace-based end-systolic stress was substantially lower than myocardial fiber stress calculated with the finite element method. This result was comparable with the study performed by Zhang and associates [40].



**Fig. 4** 3D myocardial wall stress distribution at **a** end-diastole and **b** end-systole at $Q_{mean}$ of 3.7 l/min (unit of fringe levels: hPa = 0.1 kPa)
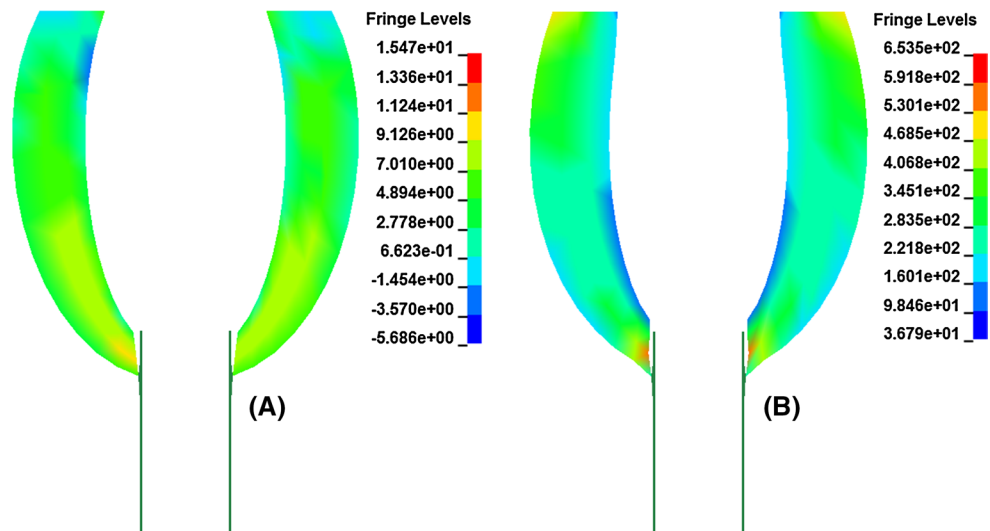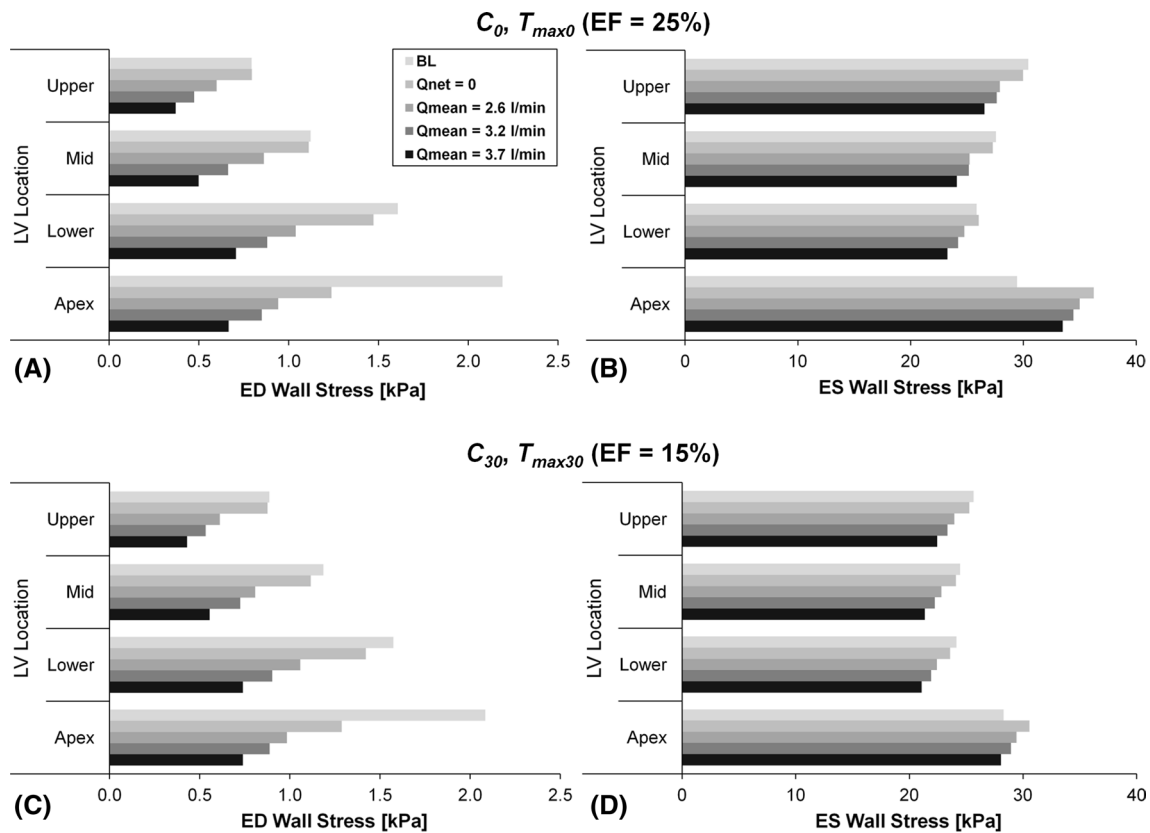
**Fig. 5 a** End-diastolic wall stress and **b** end-systolic wall stress at four regions along the long-axis direction for initial myocardial stiffness ($C_0 = 0.261$ kPa) and contractility ($T_{max0} = 126.4$ kPa). **c** End-diastolic wall stress and **d** end-systolic wall stress with further depressed myocardial compliance ($C_{30} = 0.339$ kPa) and contractility ($T_{max30} = 88.5$ kPa)

### 3.3 Sensitivity study

The amount of wall stress change by the LVAD support was not sensitive to changes in diastolic and systolic material parameters. Figure 6 shows that total wall stress reduction, $\Delta\sigma_{Total}$, at $Q_{mean}$ of 3.2 l/min did not vary significantly as a function of compliance change (Fig. 6a, b) or contractility change (Fig. 6c, d) ($p > 0.05$). The exception being at the apex, where there was an approximately 10 % variation in end-systolic wall stress for a 30 % variation in LV contractility (Fig. 6d); as $T_{max}$ decreased, end-systolic wall stress concentration at the apex was lessened; however, no statistical significance was found ($p > 0.05$).

## 4 Discussion

This study focused on the acute effect of the continuous flow LVAD support on 3D myocardial wall stress by using a computational model of the LV with apical cannulation. The primary finding of this study is that LVAD support unloads the wall stress greatest at end-diastole as compared to end-systole. Large reduction in wall stress was

observed with a moderate reduction in EDV at the lowest LVAD speed of 8,000 RPM. This might have been surprising if the wall stress were calculated by using the Laplace's law. According to Zhang and colleagues [40], Laplace's law underestimates stress in the fiber direction and fails to account for transmural stress variation. They also showed that the discrepancy between the myocardial fiber stress and averaged circumferential or longitudinal stress was more pronounced in the LV with surgical repair. The FE-based fiber stress in this study took into account not only LV volume and pressure, but also local volume change, transmural wall thickness variation, and local deformation from inner wall (sub-endocardium) to outer wall (sub-epicardium) at each finite element. Therefore, we believe the reduction in wall stress (i.e., myocardial fiber stress) provided in this study is realistic. To the best of our knowledge, this is the first study that examines the systematic effect of change in LVAD unloading on regional LV mechanics in terms of 3D myocardial fiber stress (Table 3).

There was a large reduction in LV volume and pressure at 8,000 RPM followed by lesser additional reductions at higher pump speeds. This is mainly due to the change in boundary system, i.e., the LV combined with an LVAD
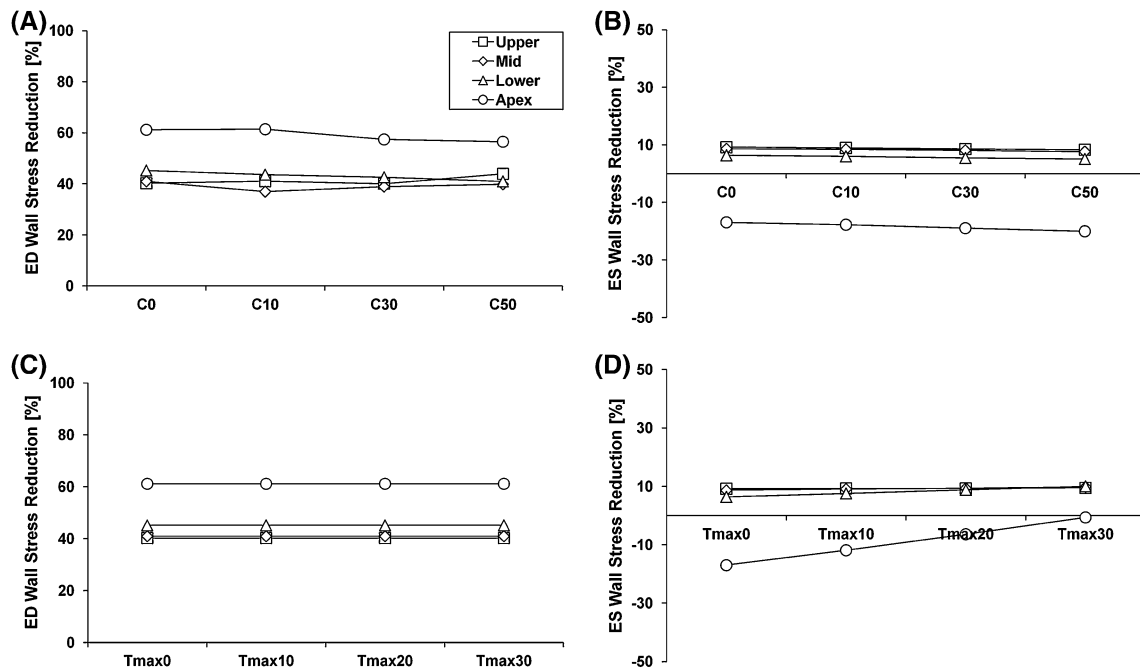
**Fig. 6** Effect of reduced compliance and contractility on the wall stress reduction by a given LVAD support ($Q_{mean} = 3.2$ l/min). Total wall stress reduction at **a** end-diastole and **b** end-systole as a function of reduced compliance where $C_0 = 0.261$, $C_{10} = 0.287$, $C_{30} = 0.339$, and $C_{50} = 0.392$ kPa. Total wall stress reduction at **c** end-diastole and **d** end-systole as a function of reduced contractility where $T_{max0} = 126.4$, $T_{max10} = 113.8$, $T_{max20} = 101.1$, and $T_{max30} = 88.5$ kPa. Similar results were shown in other LVAD supports

**Table 3** Wall stress calculated with the Laplace's law at end-diastole ($\sigma_{ED}$) and end-systole ($\sigma_{ES}$)

|  | BL | LV$_{support}$, $Q_{mean}$ (l/min) | | |
|---|---|---|---|---|
|  |  | 2.6 | 3.2 | 3.7 |
| $\sigma_{ED}$ (kPa) | 1.1 | 0.9 | 0.8 | 0.7 |
| $\sigma_{ES}$ (kPa) | 6.1 | 6.3 | 6.2 | 5.9 |

resulting in substantial changes in LV volume as well as LV chamber pressure [19]. This suggests that LVAD support itself even with minimum support substantially reduces myocardial fiber stress, and the additional reduction is proportional to the amount of support. There was no visible reduction in EDP from 8,000 RPM to 9,000 RPM that may be due to the moderate failing heart condition used in this study. According to our previous study [19], pressure and volumetric unloading for a given LVAD support depends on current heart condition, and the amount of unloading is more dominant in more depressed heart condition.

It is interesting to see a substantial increase (23 %) of apical end-systolic wall stress with EF = 25 % just due to the LVAD presence. With EF = 15 %, the relative increase of apical end-systolic wall stress was much less (8 %). Besides, this apical end-systolic wall stress was not heavily reduced with increasing LVAD support, but rather appeared

to be persistent. Recently, physicians and device industries have thought about using LVADs to prevent a less sick heart from progressing to advanced heart failure (NYHA class IV) due to favorable long-term outcomes [17]. This study suggests that definition and identification of a "less-sick" (i.e., EF > 25 %) heart may be a crucial step before applying LVADs to this patient population because of a potentially higher increase (>23 % for example) of apical end-systolic wall stress.

Although we found that the increased end-systolic wall stress at the apex was nullified by maximum LVAD support ($Q_{mean} = 3.7$ l/min), aortic valve closure also occurred. This finding suggests that the small reduction of (end-systolic) wall stress with full LVAD support may not always be clinically beneficial due to potential aortic valve fusion [23], LV atrophy [1], and valve insufficiency [24].

The use of LVADs is a major step forward in the care of end-stage heart failure patients due to their significant improvement in reduced size/weight with much simplified design and less thromboembolism. These technological advances result in improved survival rate, quality of life, and physiological capacity among recipients. Hydrodynamic and mechanical benefits of LVADs are comprised of hemodynamic unloading in LV pressure and volume, as well as kinematic constraint at the cannulated area that gives rises to additional volumetric unloading. The

kinematic constraint at the apex may generate the similar mechanism shown in other cardiac support devices (CSD) used in a passive fashion such as Acorn CorCap™ CSD [22] and Paracor HeartNet™ [20]. These synergetic effects may lead to a considerable amount of decrease in wall stress especially at end-diastole, and this may eventually initiate reverse remodeling of the LV, reducing chamber size and thickening the walls [2, 4, 27, 31, 38]. Moreover, since an LVAD affects mainly on reducing diastolic chamber pressure during support, the myocardium may try to adapt to normalize diastolic wall stress [3].

Recent studies have shown reverse remodeling after application of devices in patients with end-stage heart failure awaiting heart transplantation. They have demonstrated that LVAD support provokes regression of the myocardial dysfunction including, to name a few, improvement of distorted cardiac geometry [38], reversal of contractile dysfunction [7, 15], improvement of endothelial function [8], and restoration of the collagen network in the extracellular matrix [5]. These reverse adaptations are believed to be related to the reduced myocardial wall stress [10].

The serendipitous benefit (i.e., CSD-like effect) was achieved by the apical cannulation at end-diastole. We also observed a stress concentration at the cannulated area resulting in increased end-systolic wall stress. Indeed, decreased end-systolic wall stress during LVAD support was observed at the upper/mid/lower regions. However, the overall effect on end-systolic wall stress appeared to be canceled out due to the local stress concentration at the cannulated area. It is known that the systolic wall stress stimulates the radial growth of myocyte, and myocytes replicate sarcomere in parallel to normalize systolic wall stress resulting in LV wall thickening, geometry change (concentric hypertrophy), and loading conditions [13]. Thus, development of a smart cannula that provides kinematic compatibility during systole may be of help to further improve patient outcomes. With current apical cannula designs, the best strategy to minimize the increase in end-systolic wall stress may be maximum LVAD support while avoiding the akinesis of aortic valve.

### 4.1 Study limitations

The results presented in the study are primarily focused on the FE-based LV mechanics of the heart model during acute unloading. Therefore, the current model does not include feedback mechanisms such as reactive changes in heart rate, autonomic tone, baroreceptor, stretch, or myocardial remodeling. The material properties used in the simulations were taken from previous studies based on in vitro biaxial measurements of tissue segments under tension [34]. Thus, absolute wall stress values acquired in the study are likely to vary with different selection of material

properties. Note that numerical simulations underestimated the volumetric unloading up to 5 % at end-systole at a given maximum LVAD support (i.e., 10,000 RPM) that may have resulted in overestimation of end-systolic wall stress. The nodal constraints in the longitudinal direction applied to both the base and apex are not physiological. In practice, the apex of the left ventricle stays stationary during the cardiac cycle due to the presence of the device, while the base moves up and down. This may have overestimated the wall stress. Finally, the use of LVAD patient data (hemodynamics, echocardiography, and tissue microstructure) will significantly strengthen the clinical translation of the model. Subject to these limitations, we believe that the normalized pattern of 3D wall stress distribution in the myocardium may not significantly vary; thus, the present computational results still provide useful information on the regional distribution of the myocardial wall stress changes in end-diastole and end-systole induced by systematic variation of the LVAD support.

## 5 Conclusion

This numerical study found that the LV wall stress reduction by the continuous flow LVAD support was more prominent at end-diastole than at end-systole. Since the traditional methods for interpreting the LV mechanics derived by the force balance (i.e., Laplace's law) are insufficient to characterize the *true* wall stress especially in mechanically supported hearts, the utility of the numerical method will greatly enhance the current understanding of the LV mechanics for the LVAD recipients. This model can be used to further understand optimal unloading, pump control, design of cannula, and patient management.

## Appendix

Constitutive equations for myocardium

*Diastolic material properties*

Diastolic material properties are represented by the strain energy function, *W,* to describe the myocardium with respect to the local muscle fiber direction as,

$$W = \frac{C}{2}\Big\{ \exp\Big[ b_f E_{11}^2 + b_t(E_{22}^2 + E_{33}^2 + E_{23}^2 + E_{32}^2) \\ + b_{fs}(E_{12}^2 + E_{21}^2 + E_{13}^2 + E_{31}^2)\Big] - 1 \Big\} \quad (1)$$

where the material constant $C$ controls the myocardial stiffness, and material constants $b_f$, $b_t$, and $b_{fs}$ govern the degree

of anisotropy. $E_{11}$ is fiber strain, $E_{22}$ is cross-fiber strain, $E_{33}$ is radial strain, $E_{23}$ is shear strain in the transverse plane, and $E_{12}$ and $E_{13}$ are shear strain in the fiber-cross fiber and fiber-radial planes [34].

*Systolic material properties*

Systolic material properties are determined by defining the stress components referred to fiber coordinates. The systolic fiber stress is described as the sum of the passive stress components derived from the strain energy function $W$ and an active fiber-direction component, $T_0$, that is a function of time, $t$, peak intracellular calcium concentration, $Ca_0$, sarcomere length, $l$, and the maximum isometric tension, $T_{max}$ [34],

$$\tilde{S} = -pJ\tilde{C}^{-1} + \frac{\partial W}{\partial \tilde{E}} + T_0\{t, Ca_0, l, T_{max}\} \tag{2}$$

$\tilde{S}$ is the second Piola-Kirchoff stress tensor, $p$ is a Lagrange multiplier introducing the incompressibility constraint, and the value was adopted from the bulk modulus of heart tissue [28], $J$ is the Jacobian of the deformation gradient tensor $\tilde{F}$, $\tilde{C}$ is the right Cauchy-Green deformation tensor, and $W$ is the strain energy function in Eq. (1). A time-varying elastance model at end-systole is given by

$$T_0 = T_{max} \frac{Ca_0^2}{Ca_0^2 + ECa_{50}^2} C_t \tag{3}$$

$T_{max}$ is the maximum isometric tension achieved at the longest sarcomere length and maximum peak intracellular calcium concentration, $(Ca_0)_{max}$, and $C_t$ is given by

$$C_t = \frac{1}{2}(1 - \cos\omega), \quad \omega = \pi \frac{0.25 + t_r}{t_r}, \quad t_r = ml + b \tag{4}$$

where $m$ and $b$ are constants. The length-dependent calcium sensitivity is given by

$$ECa_{50} = \frac{(Ca)_{max}}{\sqrt{\exp\{B(l - l_0)\} - 1}}, \quad l = l_R\sqrt{2E_{ff} + 1} \tag{5}$$

where $B$ is constant, $l_0$ is the sarcomere length at which no active tension develops, and $l_R$ is the stress-free sarcomere length. Finally, the Cauchy stress tensor used to calculate myocardial fiber stress is given by

$$\tilde{\sigma} = \frac{1}{J}\tilde{F}\tilde{S}\tilde{F}^T \tag{6}$$

## References

1. Ambardekar AV, Buttrick PM (2011) Reverse remodeling with left ventricular assist devices: a review of clinical, cellular, and molecular effects. Circ Heart Fail 4(2):224–233
2. Baba HA, Grabellus F, August C, Plenz G, Takeda A, Tjan TD, Schmid C, Deng MC (2000) Reversal of metallothionein expression is different throughout the human myocardium after prolonged left-ventricular mechanical support. J Heart Lung Transplant 19(7):668–674
3. Barbone A, Oz MC, Burkhoff D, Holmes JW (2001) Normalized diastolic properties after left ventricular assist result from reverse remodeling of chamber geometry. Circulation 104(12 Suppl 1):I229–I232
4. Bruggink AH, de Jonge N, van Oosterhout MF, Van Wichen DF, de Koning E, Lahpor JR, Kemperman H, Gmelig-Meyling FH, de Weger RA (2006) Brain natriuretic peptide is produced both by cardiomyocytes and cells infiltrating the heart in patients with severe heart failure supported by a left ventricular assist device. J Heart Lung Transplant 25(2):174–180
5. Bruggink AH, van Oosterhout MF, de Jonge N, Ivangh B, van Kuik J, Voorbij RH, Cleutjens JP, Gmelig-Meyling FH, de Weger RA (2006) Reverse remodeling of the myocardial extracellular matrix after prolonged left ventricular assist device support follows a biphasic pattern. J Heart Lung Transplant 25(9):1091–1098
6. Carabello BA (1995) The relationship of left ventricular geometry and hypertrophy to left ventricular function in valvular heart disease. J Heart Valve Dis 4(Suppl 2):S132–S138 (discussion S138–S139)
7. Chaudhary KW, Rossman EI, Piacentino V 3rd, Kenessey A, Weber C, Gaughan JP, Ojamaa K, Klein I, Bers DM, Houser SR, Margulies KB (2004) Altered myocardial Ca2 + cycling after left ventricular assist device support in the failing human heart. J Am Coll Cardiol 44(4):837–845
8. Chen Y, Park S, Li Y, Missov E, Hou M, Han X, Hall JL, Miller LW, Bache RJ (2003) Alterations of gene expression in failing myocardium following left ventricular assist device support. Physiol Genomics 14(3):251–260
9. Devereux RB, Roman MJ, Palmieri V, Okin PM, Boman K, Gerdts E, Nieminen MS, Papademetriou V, Wachtell K, Dahlof B (2000) Left ventricular wall stresses and wall stress-mass-heart rate products in hypertensive patients with electrocardiographic left ventricular hypertrophy: the LIFE study. Losartan Intervention For Endpoint reduction in hypertension. J Hypertens 18(8):1129–1138
10. Drakos SG, Kfoury AG, Selzman CH, Verma DR, Nanas JN, Li DY, Stehlik J (2011) Left ventricular assist device unloading effects on myocardial structure and function: current status of the field and call for action. Curr Opin Cardiol 26(3):245–255
11. Gere JM, Goodno BJ (2009) Mechanics of materials. Cengage Learning, Mason
12. Grossman W (1980) Cardiac hypertrophy: useful adaptation or pathologic process? Am J Med 69(4):576–584
13. Grossman W, Jones D, McLaurin LP (1975) Wall stress and patterns of hypertrophy in the human left ventricle. J Clin Investig 56(1):56–64
14. Guccione JM, Moonly SM, Wallace AW, Ratcliffe MB (2001) Residual stress produced by ventricular volume reduction surgery has little effect on ventricular function and mechanics: a finite element model study. J Thorac Cardiovasc Surg 122(3):592–599
15. Heerdt PM, Holmes JW, Cai B, Barbone A, Madigan JD, Reiken S, Lee DL, Oz MC, Marks AR, Burkhoff D (2000) Chronic unloading by left ventricular assist device reverses contractile dysfunction and alters gene expression in end-stage heart failure. Circulation 102(22):2713–2719
16. Jan KM (1985) Distribution of myocardial stress and its influence on coronary blood flow. J Biomech 18(11):815–820
17. Jeevanandam V (2012) Are we ready to implant left ventricular assist devices in "less sick" patients? Semin Thorac Cardiovasc Surg 24(1):8–10
18. Jhun CS, Wenk JF, Zhang Z, Wall ST, Sun K, Sabbah HN, Ratcliffe MB, Guccione JM (2010) Effect of adjustable passive

constraint on the failing left ventricle: a finite-element model study. Ann Thorac Surg 89(1):132–137

19. Jhun C-S, Reibson JD, Cysyk JP (2011) Effective ventricular unloading by left ventricular assist device varies with stage of heart failure: cardiac simulator study. ASAIO J 57(5):407–413

20. Klodell CT Jr, Aranda JM Jr, McGiffin DC, Rayburn BK, Sun B, Abraham WT, Pae WE Jr, Boehmer JP, Klein H, Huth C (2008) Worldwide surgical experience with the Paracor HeartNet cardiac restraint device. J Thorac Cardiovasc Surg 135(1):188–195

21. La Gerche A, Heidbuchel H, Burns AT, Mooney DJ, Taylor AJ, Pfluger HB, Inder WJ, Macisaac AI, Prior DL (2011) Disproportionate exercise load and remodeling of the athlete's right ventricle. Med Sci Sports Exerc 43(6):974–981

22. Mann DL, Kubo SH, Sabbah HN, Starling RC, Jessup M, Oh JK, Acker MA (2011) Beneficial effects of the CorCap cardiac support device: Five-year results from the Acorn Trial. J Thorac Cardiovasc Surg 143(5):1036–1042

23. Martina JR, Schipper ME, de Jonge N, Ramjankhan F, de Weger RA, Lahpor JR, Vink A (2013) Analysis of aortic valve commissural fusion after support with continuous-flow left ventricular assist device. Interact CardioVasc Thorac Surg 17(4):616–624

24. Morgan JA, Brewer RJ, Nemeh HW, Henry SE, Neha N, Williams CT, Lanfear DE, Tita C, Paone G (2012) Management of aortic valve insufficiency in patients supported by long-term continuous flow left ventricular assist devices. Ann Thorac Surg 94(5):1710–1712

25. Mueller XM, Tevaearai HT, Tucker O, Boone Y, von Segesser LK (2001) Reshaping the remodelled left ventricle: a new concept. Eur J Cardiothorac Surg 20(4):786–791

26. Mueller XM, Tevaearai H, Boone Y, Augstburger M, von Segesser LK (2002) An alternative to left ventricular volume reduction. J Heart Lung Transplant 21(7):791–796

27. Remmelink M, Sjauw KD, Henriques JP, de Winter RJ, Vis MM, Koch KT, Paulus WJ, de Mol BA, Tijssen JG, Piek JJ, Baan J Jr (2010) Effects of mechanical left ventricular unloading by Impella on left ventricular dynamics in high-risk and primary percutaneous coronary intervention patients. Catheter Cardiovasc Interv 75(2):187–194

28. Saraf H, Ramesh KT, Lennon AM, Merkle AC, Roberts JC (2007) Mechanical properties of soft human tissues under dynamic loading. J Biomech 40(9):1960–1967

29. Sheikh FH, Russell SD (2011) HeartMate(R) II continuous-flow left ventricular assist system. Expert Rev Med Devices 8(1):11–21

30. Slaughter MS, Pagani FD, Rogers JG, Miller LW, Sun B, Russell SD, Starling RC, Chen L, Boyle AJ, Chillcott S, Adamson RM, Blood MS, Camacho MT, Idrissi KA, Petty M, Sobieski M, Wright S, Myers TJ, Farrar DJ (2010) Clinical management of continuous-flow left ventricular assist devices in advanced heart failure. J Heart Lung Transplant 29(4 Suppl):S1–S39

31. Smalling RW, Cassidy DB, Barrett R, Lachterman B, Felli P, Amirian J (1992) Improved regional myocardial blood flow, left ventricular unloading, and infarct salvage using an axial-flow, transvalvular left ventricular assist device. A comparison with intra-aortic balloon counterpulsation and reperfusion alone in a canine infarction model. Circulation 85(3):1152–1159

32. Streeter DD Jr, Hanna WT (1973) Engineering mechanics for successive states in canine left ventricular myocardium. I. Cavity and wall geometry. Circ Res 33(6):639–655

33. Streeter DD Jr, Hanna WT (1973) Engineering mechanics for successive states in canine left ventricular myocardium. II. Fiber angle and sarcomere length. Circ Res 33(6):656–664

34. Sun K, Stander N, Jhun CS, Zhang Z, Suzuki T, Wang GY, Saeed M, Wallace AW, Tseng EE, Baker AJ, Saloner D, Einstein DR, Ratcliffe MB, Guccione JM (2009) A computationally efficient formal optimization of regional myocardial contractility in a sheep with left ventricular aneurysm. J Biomech Eng 131(11):111001

35. Veress AI, Segars WP, Tsui BM, Gullberg GT (2011) Incorporation of a left ventricle finite element model defining infarction into the XCAT imaging phantom. IEEE Trans Med Imaging 30(4):915–927

36. Walsh RG (2005) Design and features of the acorn corcap cardiac support device: the concept of passive mechanical diastolic support. Heart Fail Rev 10(2):101–107

37. Wohlschlaeger J, Schmitz KJ, Schmid C, Schmid KW, Keul P, Takeda A, Weis S, Levkau B, Baba HA (2005) Reverse remodeling following insertion of left ventricular assist devices (LVAD): a review of the morphological and molecular changes. Cardiovasc Res 68(3):376–386

38. Zafeiridis A, Jeevanandam V, Houser SR, Margulies KB (1998) Regression of cellular hypertrophy after left ventricular assist device support. Circulation 98(7):656–662

39. Zhang J, Narula J (2004) Molecular biology of myocardial recovery. Surg Clin North Am 84(1):223–242

40. Zhang Z, Tendulkar A, Sun K, Saloner DA, Wallace AW, Ge L, Guccione JM, Ratcliffe MB (2011) Comparison of the young-Laplace law and finite element based calculation of ventricular wall stress: implications for post infarct and surgical ventricular remodeling. Ann Thorac Surg 91(1):150–156